Infrared Physics and Technology 99 (2019) 178–186

Contents lists available at ScienceDirect

Infrared Physics & Technology

journal homepage: www.elsevier.com/locate/infrared

Regular article

A grayscale weight with window algorithm for infrared and visible image registration

Kun Yu, Jie Ma*, Fangyu Hu, Tao Ma, Siwen Quan, Bin Fang

School of Artificial Intelligence and Automation, Huazhong University of Science and Technology, Wuhan 430074, China
National Key Laboratory of Science and Technology on Multispectral Information Processing, Huazhong University of Science and Technology, Wuhan 430074, China

ARTICLE INFO

Keywords:
Infrared and visible image registration
Normalized mutual information
Mutual information
Entropy correlation coefficient
Grayscale weight with window algorithm

ABSTRACT

The registration of Infrared (IR) and visible images is an important prerequisite for image processing tasks such as image fusion, target detection and tracking, and remote sensing. The registration task of the IR and visible images usually involves two problems: (1) extracting consistent features from multi-sensor images is difficult and (2) similarity measurement methods such as normalized mutual information (NMI) algorithms are prone to falling into local extremities. To solve these complications, this study proposes a grayscale weight with window algorithm (GWW) to extract common strong edge features from IR and visible images, reduce the joint entropy values and local extreme values of NMI, and improve the performance of NMI to calculate IR and visible images for registration. Qualitative and quantitative experiments demonstrate that the GWW can effectively extract the common features of IR and visible image pairs, improve the performance of the surface peak, increase the ratio of primary and secondary peaks, and effectively reduce the local extremum. The performance of NMI combined with the GWW algorithm is better than the traditional MI, NMI, and ECC, and has better matching accuracy and higher matching probability. The registration of IR and visible images can be fully realized by NMI combined with the GWW algorithm.

1. Introduction

The comprehensive use of multi-sensor images for data extraction and information analysis is extremely important in the field of modern information processing. The imaging effects of multi-sensor images vary due to differences in imaging principles, imaging platforms, and operating wave length ranges of various imaging sensors, such as IR images and visible images. The registration of IR and visible images should match image pairs under different conditions. The main purpose is to match the IR image to the visible image coordinate system through an algorithm so that the image pixels can establish the corresponding ship. The registration of IR and visible images is an important prerequisite for image processing tasks such as image fusion [1–5], image target detection and tracking [6–8], and remote sensing [9,10]. For example, IR images can provide a target's heat source radiation information in the scene, and visible light can provide complex and detailed scene information. The fusion of the two datasets can comprehensively describe the spatial information of a target object. The prerequisite of IR and visible image fusion is to achieve strict registration of the geometric position and gray levels through data extraction and the analysis of IR and visible images. Thus, this is a popular topic of research in the field of IR and visible image registration.

An IR image mainly reflects the radiation intensity of the target, which differs from the visible image. There is an inversion of the pixel grayscale between an infrared image and a visible image (see the red[1] and yellow boxes in Fig. 1), and the common feature extraction from IR and visible image pairs is difficult due to the different imaging sensors. Therefore, significant errors can occur when calculating the entropy distribution of registration region images via direct similarity measurement methods, which complicates registration.

IR and visible image registration methods are classified into two categories: feature-based and area-based methods. Feature-based methods first extract two sets of salient structures from the IR and visible image pairs. The structures are comprised of feature points [9,11,12], feature lines [13], and feature edges [14,15]. This method determines the correct correspondence between the images and estimates the spatial transformation accordingly, thereby aligning the given image pairs. Area-based methods directly process the intensity of IR and visible image pairs. If the salient details in the IR and visible image pairs are insufficient and the prominent information is provided

* Corresponding author.
E-mail address: majie@hust.edu.cn (J. Ma).
[1] For interpretation of color in Figs. 1 and 3, the reader is referred to the web version of this article.

https://doi.org/10.1016/j.infrared.2019.04.021
Received 17 December 2018; Received in revised form 6 March 2019; Accepted 22 April 2019
Available online 22 April 2019
1350-4495/

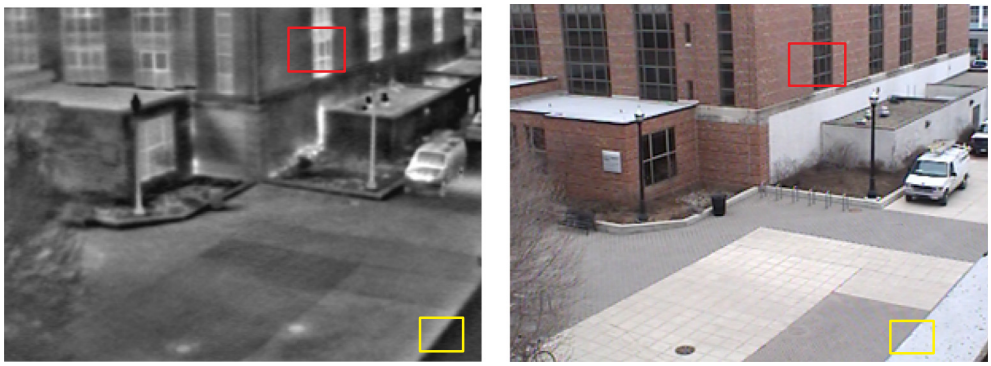

Fig. 1. Schematic diagram of gray inversion of IR and VIS image.

by the intensity of the pixels rather than the prominent structure, they are affected by image illumination changes and computational complexity; in this case, area-based methods are preferable. These methods are superior because the grayscale image information is fully utilized without detecting the corresponding features. There are three major types of area-based methods; Fourier [16], correlation-like [17], and mutual information (MI) [18–21].

Viola [22] first introduced mutual information to measure the statistical dependence between two grayscale image statistical variables in the field of multi-modal image registration. Because MI is not sensitive to grayscale differences between images, it has advantages such as high precision and significant robustness. Some research on MI found that it does not have overlapping invariance. Studholme [23] studied normalized mutual information (NMI) based on MI and confirmed that NMI has overlapping invariance. Maes [24] proposed an improved entropy correlation coefficient (ECC) method based on MI. The outstanding performance of the NMI algorithm in registration, has generated substantial research and application.

Park et al. [25] proposed an image fusion algorithm using the traditional NMI algorithm in IR and visual vision systems. The proposed method consists of the extraction and comparison of feature points, image registration, and pseudo-colors for display. This method compares feature points detected from multi-sensors using the traditional NMI algorithm. Although the proposed algorithm can detect some common feature points in IR and visible image pairs, it is not very effective when most of the image feature points are inconsistent.

Kim et al. [26] proposed two preprocessing schemes to improve the performance of NMI-based registration to manage the robust registration of multi-sensor images. One method, the extraction of statistically correlated regions, extracts the regions in electro-optic images that are highly correlated to the corresponding IR image regions, and the extracted regions are used to calculate the NMI. By applying these preprocessing methods, the NMI curve smoothly varies and has a maximum value when a pair of images is exactly aligned. However, the primary peak is not prominent, and it is easy to produce local extremum to affect the registration robustness.

Because the traditional NMI algorithm can produce local extremum for IR and visible image registration, Bai et al. [27] proposed an improved gradient NMI algorithm. This algorithm simply multiplies the NMI result by a gradient term, including the gradient size and direction. The proposed algorithm only considers eliminating the multi-peak condition, but does not ameliorate the low correlation between IR and visible images. Although the gradient has certain similarities, if the IR and visible image pair with a gray inversion area due to an image pair reflecting different properties are directly calculated by NMI, the registration position of the IR and the visible image pair may not be accurate.

To overcome the inconsistencies in the common features of the IR and visible image pairs due to the gray inversion of multi-sensor images, and because traditional NMI are prone to producing more local extremum that affect the registration robustness, we propose a grayscale weight with window algorithm (GWW). The purpose of the proposed algorithm is to extract common strong edge features from the IR and visible images to reduce the joint entropy values and local extreme values of the NMI and improve the its performance to calculate the IR and visible images for registration, so the registration of the IR and visible images will produce more accurate results. The proposed algorithm consists of three steps: (1) An $N \times N$ window is establish from the source image. A circle is drawn with the center $g(x_c, y_c)$ of the window as the circle center and r as the radius. We sample on the circle to obtain uniform P pixels. After calculating the mean gray $g_{mean}(x, y)$ of the pixels, the ratio R between the mean value $g_{mean}(x, y)$ and the gray value of the center point $g(x_c, y_c)$ is obtained. (2) The ratio R as the judgment value of the gray stability and compare it with one. According to the value of R, different values of α are used as weighted coefficients. A new gray value $g'(x_c, y_c)$ is multiplied by the center gray $g(x_c, y_c)$ by the weight α. (3) After the window traverses the calculated source image, the image $H(x, y)$ is extracted from the source image, and the final feature image $I(x, y)$ is obtained by normalizing $H(x, y)$.

This paper is organized as follows: Section 2 briefly introduces several traditional algorithms for similarity measurement, including MI, NMI, and ECC. The proposed algorithm based on NMI is described in detail. The contrast of the edge features between the GWW and other algorithms is provided. Section 3 presents the qualitative and quantitative experimental results and analysis. Section 4 is the conclusion.

2. Methodology

2.1. Similarity measurement method

Normalized mutual information is designed to manage the partial overlap of images based on MI. NMI is defined in Eq. (1). $NMI(A, B)$ is the ratio of the edge entropy to the joint entropy, and the increase in the edge entropy is constrained by the increase in the joint entropy. When it approaches the registration, the joint entropy of the image decreases gradually, and the $NMI(A, B)$ increases. When the contents of the two images are completely identical and the normalized mutual information reaches the registration position, the edge entropy and joint entropy in the overlapping region are equal, and the normalized mutual information value is the maximum value.

$$NMI(A, B) = \frac{H(A) + H(B)}{H(A, B)} \tag{1}$$

where $H(A)$ and $H(B)$ denote the entropy values of image A and image B, respectively.$H(A, B)$ is the entropy of the joint probability distribution of image A and image B. The calculation relationship between NMI and MI is defined as Eq. (2). The calculation relationship between NMI and ECC is defined as Eq. (3).

$$MI(A, B) = H(A, B)\cdot(NMI(A, B) - 1) \tag{2}$$

$$ECC(A, B) = 2 - \frac{2}{NMI(A, B)} \tag{3}$$

The entropy values are calculated using Eqs. (4)–(6).

$$H(A) = -\sum_{a} p_A(a) \log p_A(a) \tag{4}$$

$$H(B) = -\sum_{b}^{a} p_B(b) \log p_B(b) \tag{5}$$

$$H(A, B) = -\sum_{a,b}^{b} p_{A,B}(a, b) \log p_{A,B}(a, b) \tag{6}$$

where $p_A(a)$ and $p_B(b)$ are the marginal probability densities, $p_{A,B}(a, b)$ is the joint probability density. The minus sign ensures that the entropy value is not negative. The entropy values $H(A)$ is a measure of the uncertainty of random variable $p_A(a)$, and it is the expectation of the amount of information generated by all possible events. The joint probability $H(A, B)$ distribution is the marginal probability distribution of combining two images. Assuming that two images are combined into one image, different gray levels of the composite image represent different pixel pairs corresponding to the overlapped positions. Therefore, when the feature information of two images is closer, the similarity measurement results of the NMI algorithm are more accurate.

2.2. Our proposed algorithm

To improve the NMI algorithm's performance, we propose a local grayscale difference weight algorithm with windows. The algorithm flow chart is shown in Fig. 2.

In our proposed algorithm, we first establish a $N \times N$ window in the source image. A circle is drawn with the center $g(x_c, y_c)$ of the window as the circle center, and r as the radius. We can sample the pixels on the circle evenly, the radius r and the number of sampling points P can be defined as Eqs. (7) and (8).

$$r = \frac{\mathrm{N}-1}{2} \tag{7}$$

$$P = 4(\mathrm{N}-1) \tag{8}$$

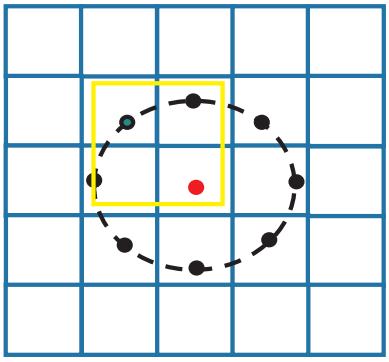

Fig. 3. Schematic diagram of non-integer point pixels.

Since there are non-integer point pixels in the circular box such as green point $g(x_{p_i}, y_{p_i})$ in Fig. 3, the bilinear difference method can be used to calculate the gray value of the non-integer position. The coordinates of the non-integer points are calculated using Eqs. (9) and (10).

$$x_{p_i} = x_c + r \times \cos\left(\frac{2\pi p_i}{P}\right), \ i = 1, 2, \cdots, P \tag{9}$$

$$y_{p_i} = y_c - r \times \sin\left(\frac{2\pi p_i}{P}\right), \ i = 1, 2, \cdots, P \tag{10}$$

where p_i represents the number of current points. The gray value of the non-integer points such as $g(x_{p_i}, y_{p_i})$ is calculated using the weighted average of the gray value of the surrounding three points (see the yellow box in Fig. 3).

The mean gray $g_{mean}(x, y)$ of all of the sampling points on the circle is calculated. The ratio R of the mean gray $g_{mean}(x, y)$ to the center point gray $g(x_c, y_c)$ of the window can be defined by Eq. (11).

$$R = \frac{g_{mean}(x, y)}{g(x_c, y_c)} \tag{11}$$

As shown in Eq. (8), we use the ratio R as the judgment value of gray stability and compare it with one. According to the results of the R value calculation, different weights α will be used to judge different R

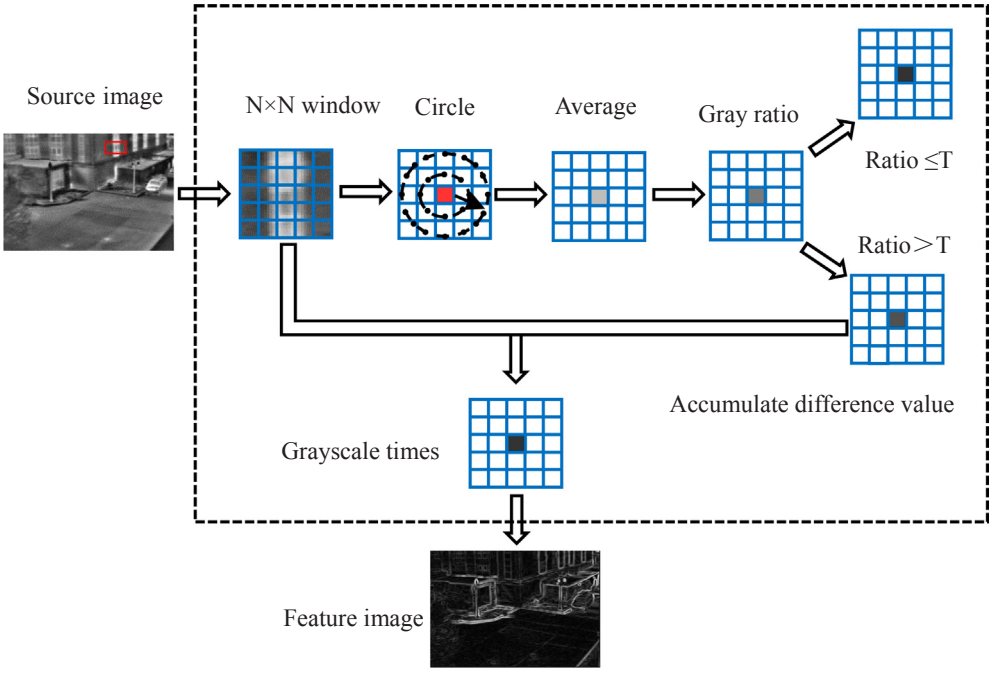

Fig. 2. Our proposed algorithm flow chart.

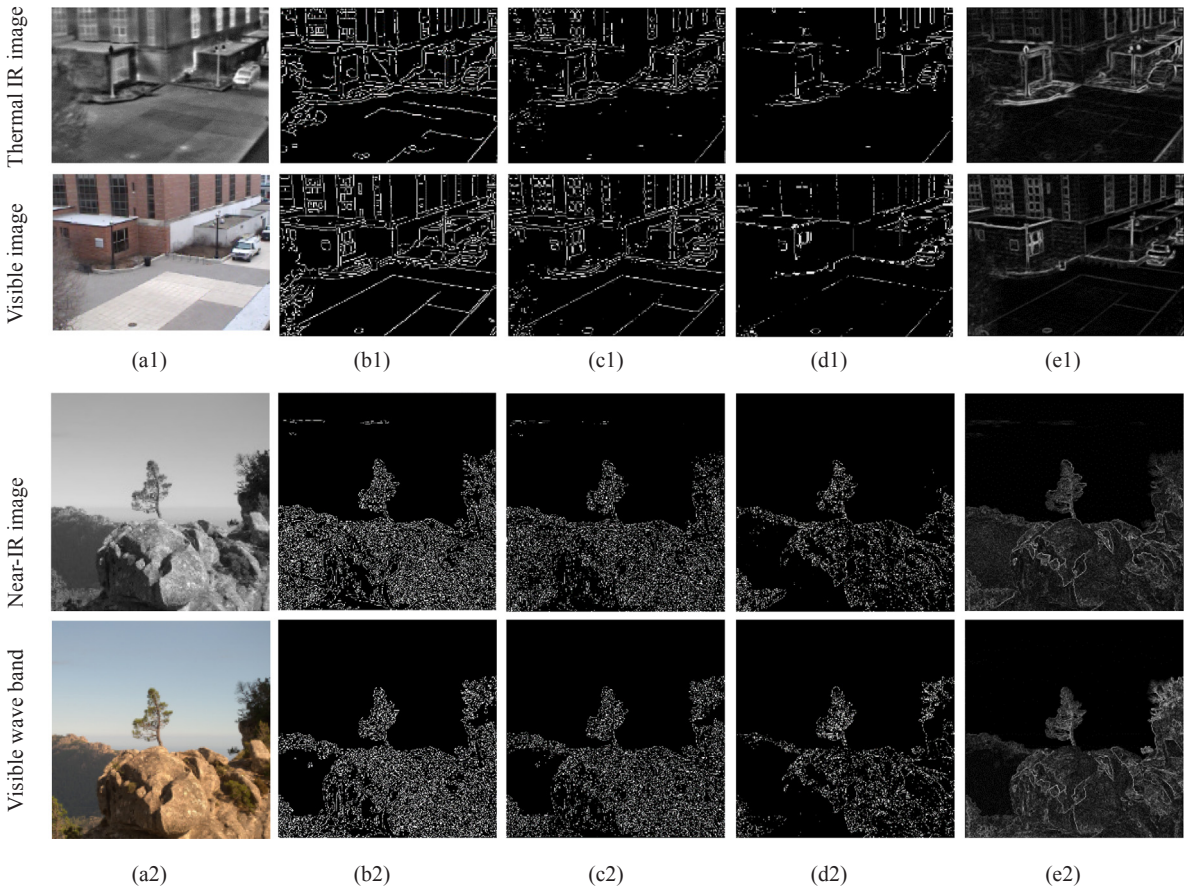

Fig. 4. Edge feature images of IR image and visible image. (a) Source images, (b) Canny feature images, (c) LoG feature images (d) Sobel feature images, and (e) GWW algorithm feature images.

Fig. 5. The dataset of IR and visible images. (a) Building, (b) Country, (c) Urban, and (d) Water.

values. The conditional judgment formula can be defined as Eq. (12)

$$g'(x_c, y_c) = \begin{cases} \alpha \cdot g(x_c, y_c), & R > 1 \\ 0, & R \leqslant 1 \end{cases} \tag{12}$$

When R is less than one, the mean gray value of all of the sampling pixels on a circle equidistant from the center point is less than the gray value of the center point. We assign the weight α value to be 0, so that the new gray value $g'(x_c, y_c)$ is 0. This is to reduce the width of the edge, so that the strong edge is more obvious with a better degree of differentiation. In particular, when R is equal to one, the mean gray level $g_{mean}(x, y)$ is the same as the center gray level $g(x_c, y_c)$, so that the gray value of the background in the window remains basically the same without edge features, so that the new gray value $g'(x_c, y_c)$ equals 0. When R is greater than one, we multiply the center gray level $g(x_c, y_c)$ by the weight α as the new grayscale $g'(x_c, y_c)$. The weight α value can be defined as Eq. (13)

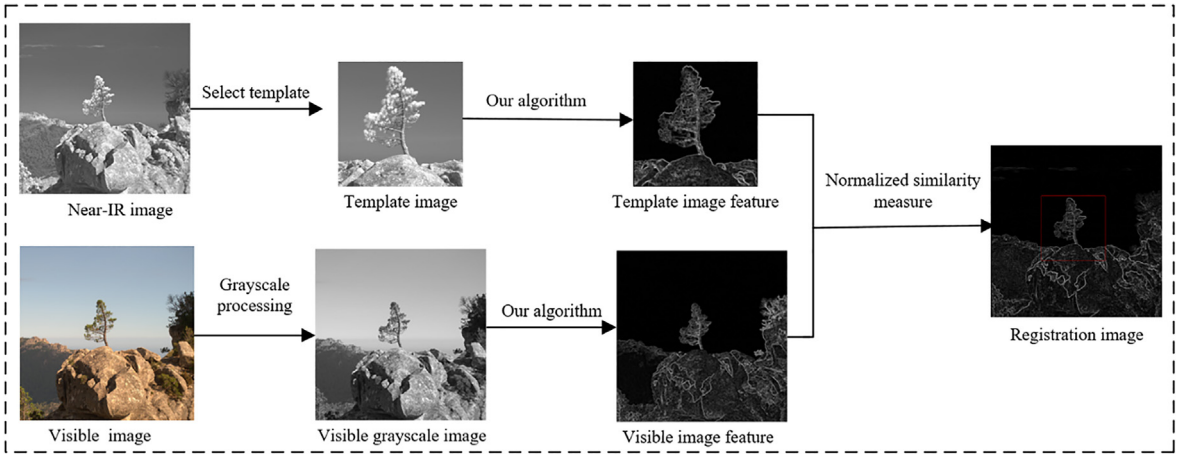

Fig. 6. Schematic diagram of IR and visible image registration process.

$$\alpha = \frac{1}{P}\sum_{i=1}^{P}\frac{|g_i(x,y) - g_{mean}(x,y)|}{\max\{g_i(x,y), g_{mean}(x,y)\}} \tag{13}$$

where P is the number of uniform sampling points and $g_i(x, y)$ is the gray value of the current sampling point. When the grayscale of the sampling points in the window changes sharply, it means that there is a strong edge feature in the window. The weight α is an accumulative value, and its size reflects the degree of characterization of the strong edges.

Therefore, a new gray value $g'(x_c, y_c)$ is obtained to replace the original gray value of the window center point $g(x_c, y_c)$. After the window traverses the calculated image, the strong edge feature information $H(x, y)$ can be extracted from the source image. The gray level of $H(x, y)$ may not fill the entire value range of 0–255. Thus, to highlight the difference between the strong edges and the weak edges, the data grayscale method is used to process the gray level of $H(x, y)$. The data grayscale method is defined by Eq. (14).

$$I(x,y) = (255 - 0) \times \frac{H(x,y) - H_{\min}}{H_{\max} - H_{\min}} \tag{14}$$

where $H_{\min}$ is the minimum gray value in $H(x, y)$, $H_{\max}$ is the maximum gray value in $H(x, y)$, and $I(x, y)$ is the feature image processed by our algorithm.

2.3. Algorithm effect comparison

Our proposed algorithm is compared with the three other contour feature extraction algorithms. As Fig. 4 demonstrates, the edge algorithms such as Canny [28], LoG [29], and Sobel [30] can extract the edge features from the image pairs, but the feature distribution is not consistent. For example, some main features are extracted from the image pairs, but the corresponding positions in the visible image have no features. The strong edge and the small weak edge are also characterized and cannot be effectively distinguished, which will affect the accuracy of the joint entropy calculation in the similarity measurement NMI.

The significant comment features can be effectively preserved in the edge image using our proposed algorithm, and the common strong edges are extracted in IR and the visible image pair and the near-IR and visible image pair. At the same time, the weak edges are suppressed. After processing the image pairs using our algorithm, the feature space distribution is consistent. The strong edges and small weak edges are clearly distinguished, the difference in the gray level between the IR image and the visible image in the region is reduced, and the matching performance between the IR image and the visible image improves.

3. Experimental results and discussion

3.1. Dataset and registration process

In this experiment, we conducted qualitative and quantitative tests on IR and visible image pairs to evaluate the effectiveness of our method. All of the image pairs in the different scenes shown in Fig. 5 are from the dataset [31]. The IR and visible image pairs are shown from the same perspective. We do not need to consider the angle transformation of the image pairs, but need to measure only the registration effect.

To demonstrate the performance of our proposed algorithm, the registration process we adopted is shown in the Fig. 6. For example, in the IR image and visible image registration experiment, because the IR image and visible image record different detail information, the registration directly will have a large probability of mismatching. The template image can be selected from the IR image. After the template image and visible image are processed using our proposed algorithm respectively, the corresponding feature image is obtained, the flow is shown in Fig. 6. By extracting the feature space from the IR and visible image, the similarity degree between the strong edge features improves, and the interference of the weak edge to registration is reduced. After calculating the features of the template image and the visible image using the similarity measurement method, the registration of the IR and visible image pairs is realized by searching the space position corresponding to the maximum value of the similarity measurement result.

3.2. Qualitative evaluation of the registration results

To qualitatively evaluate the performance of our proposed algorithm, the traditional three methods (MI, NMI, and ECC) and these three methods combined with our proposed algorithm, a total of six methods are used to calculate the four IR and visible image pairs, the normalized distribution of the similarity measurement results are shown in Fig. 7. The coordinate positions and size of the four groups of template images selected from IR images are shown in Table 1.

Fig. 7 presents the comparisons of the normalized similarity measurement results of the four IR and visible image pairs. We usually look for the principal peak coordinate of the surface as the registration coordinate of the template image in the visible image. Fig. 7(a1)–(a3), Fig. 7(b1)–(b3), Fig. 7(c1)–(c3), and Fig. 7(d1)–(d3) demonstrate that the similarity measurement surface has a principal peak, that is sometimes not obvious. This is mainly because a large number of small and weak edges complicate the registration background, which greatly affects the correct description of the strong edges. The similarity measurement surfaces of the NMI and ECC have a certain degree of similarity, and the performance is better than the MI. Sometimes, the true

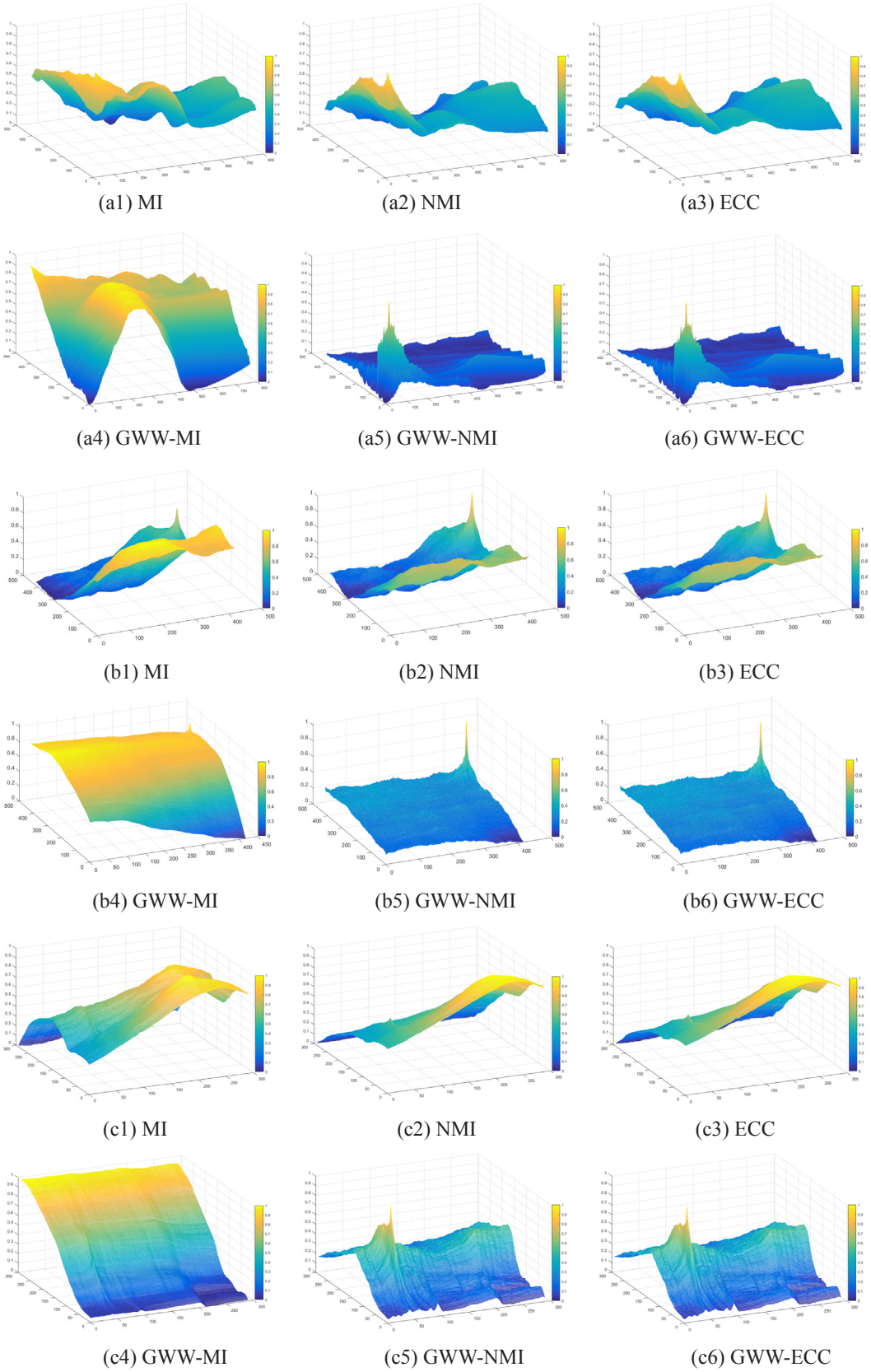

Fig. 7. Qualitative comparisons of the normalized similarity measurement results of the four IR and visible image pairs. (a) Building, (b) Country, (c) Urban, and (d) Water. From 1 to 6: MI, NMI, ECC, GWW-MI, GWW-NMI and GWW- ECC.

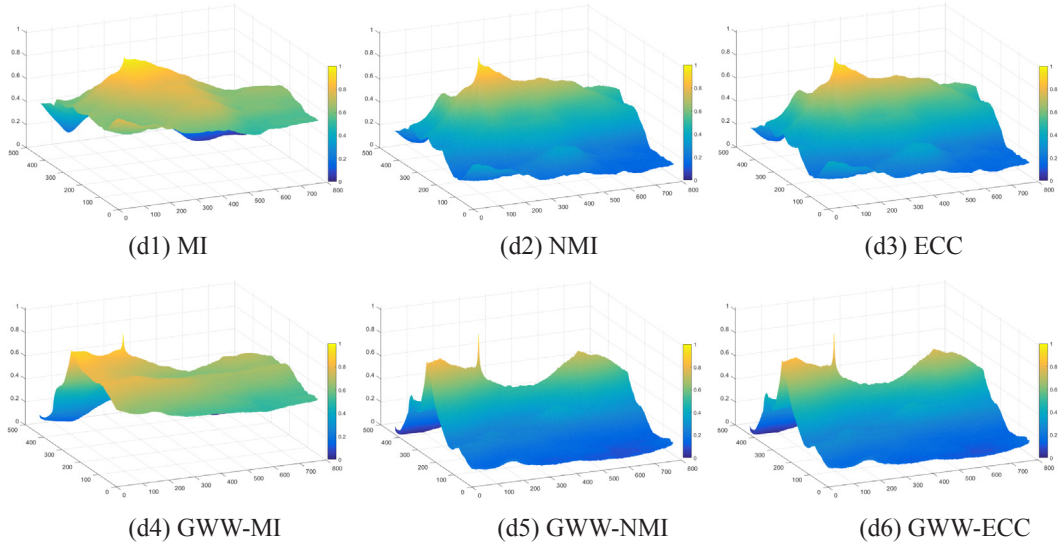

Fig. 7. (*continued*)

Table 1
Algorithm performance evaluation using the sharpness of the primary peak.

Template image	Coordinate in the IR image	Size	Area of the primary peak at 2σ/pixels					
			MI	NMI	ECC	GWW + MI	GWW + NMI	GWW + ECC
a	(50,50)	256 × 256	23	10	13	66	**4**	4
b	(350,400)	256 × 256	5865	4	4	5606	**4**	4
c	(100,50)	256 × 256	945	3149	3770	4404	**3**	4
d	(250,200)	256 × 256	542	9	11	3	**1**	1

Table 2
Algorithm performance evaluation using the ratio of the primary peak to the secondary peak.

Template image	Ratio of the primary peak to the secondary peak					
	MI	NMI	ECC	GWW + MI	GWW + NMI	GWW + ECC
a	1.04	1.08	1.08	1.02	**1.34**	1.28
b	0.82	1.30	1.28	1.01	**1.78**	1.75
c	1.01	1.94	1.86	1.05	**1.30**	1.26
d	1.03	1.08	1.09	1.10	**1.21**	1.18

Table 3
Algorithm performance evaluation using matching probability p_c

Template image	Matching probability p_c/%					
	MI	NMI	ECC	GWW + MI	GWW + NMI	GWW + ECC
a	75	82	81	74	**93**	91
b	76	84	82	76	**92**	90
c	72	78	78	82	**96**	95
d	80	80	80	78	**84**	84

Table 4
Algorithm performance evaluation using matching precision δ

Template image	Matching precision δ/pixels					
	MI	NMI	ECC	GWW + MI	GWW + NMI	GWW + ECC
a	0.081	0.070	0.070	0.052	**0.039**	0.040
b	0.078	0.052	0.059	0.074	**0.042**	0.049
c	0.064	0.061	0.061	0.054	**0.041**	0.046
d	0.062	0.066	0.066	0.058	**0.051**	0.053

principal peak of the NMI and ECC surface is even smaller than other local extremum as shown in Fig. 7(c2) and (c3), which will submerge the position of the principal peak in the local extremum. In addition, there are many other local peaks, which means that the template image has many similar feature regions in the reference image. The more regions with local peaks, the more likely there is mismatching and the more difficult it is to complete the correct IR and visible image registration. Therefore, it is necessary to extract the strong edge feature space for the IR and visible images and reduce the interference of the irrelevant weak edge features.

Our proposed algorithm can overcome the aforementioned drawbacks and achieve good performance for IR and visible image registration. As demonstrated in Fig. 7(a4)–(a6), Fig. 7(b4)–(b6), Fig. 7(c4)–(c6), and Fig. 7(d4)–(d6), the principal peak of similarity measurement surface is more obvious. Compared with the traditional MI, NMI, and ECC, the principal peaks calculated using the NMI and ECC combined with our algorithm are sharper and more prominent, and the number of local extremum is greatly reduced as shown in Fig. 7(a5), (b5), and (c5). Therefore, the principal peak coordinate is more easily determined, the registration position based on the principal peak is more accurate, and the registration probability is greatly improved. At the same time, we also intuitively observe that the NMI and ECC combined with our algorithm is better than the others.

3.3. Quantitative evaluation of the registration results

Since the similarity measurement results have been normalized, it is meaningless to compare and analyze the value of the primary peaks (see Fig. 7). The performance of each algorithm around the area of the primary peak at 2σ and the ratio of the primary peak to the secondary peak are shown in Tables 1 and 2. The best results are set in bold. The sharpness of the primary peak in the surface of the similarity measurement will affect the registration positioning accuracy. To better

(a) (b) (c) (d)

Fig. 8. The registration results on four image pairs. (a) Building, (b) Country, (c) Urban, and (d) Water.

describe the sharpness of the primary peak, we calculate the pixel area of the section where the primary peak value is 2σ ($2\sigma \approx 0.9544$). The smaller the pixel area, the sharper the main peak. As shown in Table 1, the MI, NMI, and ECC combined with our algorithm performed better than the MI, NMI, and ECC, respectively. In the four groups of experiments, the NMI areas combined with our algorithm were the smallest each time, which means that the primary peak calculated in this way has the highest sharpness and the positioning accuracy of matching is superior.

The ratio of the primary and secondary peaks can describe the repeated pattern of registration. The higher the ratio value, the greater the gap between the primary peak and the secondary peak, and the higher the confidence of the matching result. In Table 2, the ratio values calculated using the MI, NMI, and ECC combined with our algorithm are significantly improved in general, and the ratio values calculated using the NMI combined with our algorithm are significantly larger than the other methods. Thus, the robustness of the NMI combined with our algorithm is superior.

In addition to the aforementioned evaluation criteria, the performance of our algorithm would be evaluated by the reliability index (matching probability p_c) and the accuracy index (matching precision δ). Matching probability p_c can be defined by Eq. (15).

$$p_c = \frac{n_R}{n_T} \tag{15}$$

where n_R is the number of correct matches and n_T is the total number of matches. A correct match means that the match result is within the required error range. Generally, the error range is 3 pixels. The higher the matching probability, the better the matching reliability of the algorithm.

Suppose the ideal matching position coordinate is (x_i, y_i) and the actual matching position is (x_i', y_i'). Thus, the single matching error can be described as Eq. (16).

$$\delta_i = \sqrt{(x_i' - x_i)^2 + (y_i' - y_i)^2} \tag{16}$$

For n matching results, the matching precision δ is calculated using Eq. (17). The matching precision δ is calculated only when the actual matching position of a single time is within the required error range, which is not a simple statistic of all matching results.

$$\delta = \frac{1}{n}\sum_{i=1}^{n} \delta_i \tag{17}$$

We randomly selected 200 sets of template images which size is 256 * 256 from four sets of IR images for registration in visible images. The matching probability p_c and matching precision δ are illustrated in Tables 3 and 4. The best results are set in bold. From the results of matching probability p_c, NMI and ECC are combined with our algorithm have higher value, which means better reliability. Meanwhile, the NMI and ECC combined with our algorithm have smaller values than the others, which improves the positioning accuracy.

The registration result of the NMI combined with our algorithm is shown in Fig. 8. Each result is presented with an inverted checkerboard overlay. The figure demonstrates that the improved algorithm can achieve a good registration effect.

4. Conclusion

In this paper, to overcome the inconsistences in the common features of the IR and visible image pairs due to the gray inversion of the IR and visible images, and because traditional NMI are prone to producing more local extremum that affect the registration robustness, we propose a grayscale weight with window algorithm (GWW). The qualitative and quantitative experiments show that the proposed algorithm can effectively extract the common features of the IR and visible image pairs, improve the performance of the surface peak, increase the ratio of the primary and secondary peaks, and effectively reduce the local extremum. The performance of the NMI combined with the GWW algorithm is superior to the traditional MI, NMI, and ECC and has better matching accuracy and higher matching probability. The registration of the IR and visible images can be fully realized by NMI combined with the GWW algorithm.

Conflict of interest

The authors declare that there is no conflict of interest.

Acknowledgements

This work was supported by the Shanghai Aerospace Science and Technology Innovation Foundation [Grant No. SAST2016063].

References

[1] M. Tao, M. Jie, B. Fang, et al., Multi-scale decomposition based fusion of infrared and visible image via total variation and saliency analysis, Infrared Phys. Technol. (2018).
[2] X. Li, S.Y. Qin, Efficient fusion for infrared and visible images based on compressive sensing principle, Iet Image Process. 5 (2) (2011) 141–147.
[3] J. Ma, C. Chen, C. Li, et al., Infrared and visible image fusion via gradient transfer and total variation minimization, Inform. Fusion 31 (C) (2016) 100–109.
[4] C.H. Liu, Y. Qi, W.R. Ding, Infrared and visible image fusion method based on saliency detection in sparse domain, Infrared Phys. Technol. 83 (2017) 94–102.
[5] J. Ma, Y. Ma, C. Li, Infrared and visible image fusion methods and applications: a survey, Inform. Fusion (2018) S1566253517307972.
[6] P. Zhao, P.U. Zhao-Bang, T.W. Zhang, Fusion and tracking for IR and visible images, Opto-Electron. Eng. (2005).
[7] J. Song, L. Lei, H. Wei, et al., Target detection via HSV color model and edge gradient information in infrared and visible image sequences under complicated background, Opt. Quant. Electron. 50 (4) (2018) 175.
[8] J. Nie, S. Qu, Y. Wei, et al., An infrared small target detection method based on multiscale local homogeneity measure, Infrared Phys. Technol. 90 (2018) S1350449517305078.
[9] J. Ma, H. Zhou, J. Zhao, et al., Robust feature matching for remote sensing image registration via locally linear transforming, IEEE Trans. Geosci. Remote Sens. 53 (12) (2015) 6469–6481.
[10] A. Wong, D.A. Clausi, ARRSI: automatic registration of remote-sensing images, IEEE Trans. Geosci. Remote Sens. 45 (5) (2007) 1483–1493.
[11] S. Paul, U.C. Pati, Remote sensing optical image registration using modified uniform robust SIFT, IEEE Geosci. Remote Sens. Lett. 13 (9) (2016) 1300–1304.
[12] D. Yu, F. Yang, C. Yang, et al., Fast Rotation-free feature based image registration

using improved N-SIFT and GMM based parallel optimization, IEEE Trans. Biomed. Eng. 63 (8) (2016) 1653–1664.
[13] Z.L. Song, S. Li, T.F. George, Remote sensing image registration approach based on a retrofitted SIFT algorithm and Lissajous-curve trajectories, Opt. Express 18 (2) (2010) 513–522.
[14] S.K. Yong, J.H. Lee, J.B. Ra, Multi-sensor image registration based on intensity and edge orientation information, Pattern Recogn. 41 (11) (2008) 3356–3365.
[15] J. Zheng, J. Tian, K. Deng, et al., Salient feature region: a new method for retinal image registration, IEEE Trans. Inf Technol. Biomed. 15 (2) (2011) 221–232.
[16] R.N. Bracewell, The Fourier transform and its applications, Electron. Power 11 (10) (2009) 357.
[17] Z. Feng, Q. Huang, G. Wen, Image matching by normalized cross-correlation, in: IEEE International Conference on Acoustics, 2013.
[18] W.G. Qin, A.H. Gao, Real-time registration architecture for far infrared and visible image using mutual information, Adv. Mater. Res. 129–131 (2010) 328–332.
[19] Y. Sun, W. Fei, IR/visible image registration based on edge characteristics and mutual information, Electronic Sci. Technol. (2010).
[20] G. Panin, Mutual information for multi-modal, discontinuity-preserving image registration, Automatica 41 (8) (2012) 1313–1321.
[21] Y. Kuang, J. Wang, L. Peng, infrared and visible image registration by combination of second-order mutual information and alignment, Electronic Sci. Technol. (2011).
[22] Paul A. Viola, Alignment by maximization of mutual information, Int. J. Comput. Vision 24 (2) (1997) 137–154.
[23] C. Studholme, D.L.G. Hill, D.J. Hawkes, An overlap invariant entropy measure of 3D medical image alignment, Pattern Recogn. 32 (1) (1999) 71–86.
[24] F. Maes, A. Collignon, D. Vandermeulen, G. Marchal, P. Suetens, Multimodality image registration by maximization of mutual information, IEEE Trans. Med. Imaging 16 (1997) 187–198.
[25] C. Park, K. Bae, J.H. Jung, Image fusion in infrared image and visual image using normalized mutual information, in: Proceedings of SPIE – The International Society for Optical Engineering, 2008, 6968:69681Q-69681Q-9.
[26] K.S. Kim, J.H. Lee, J.B. Ra, Robust multi-sensor image registration by enhancing statistical correlation, International Conference on Information Fusion, IEEE, 2006.
[27] L. Bai, J. Han, Y. Zhang, et al., Registration algorithm of infrared and visible images based on improved gradient normalized mutual information and particle swarm optimization, Infrared Laser Eng. 41 (1) (2012) 248–254.
[28] F.F. Zhou, W.D. Chen, L.I. Liang-Fu, Canny edge based registration algorithm of IR and visible images, J. Appl. Opt. 30 (4) (2009) 605–609.
[29] S. Haralick, L. Shapiro, Computer and Robot Vision vol. 1, (1992) 346–351.
[30] J. Kim, S. Hong, J. Baek, et al., Autonomous vehicle detection system using visible and infrared camera, International Conference on Control, (2012).
[31] < https://ivrl.epfl.ch/research-2/research-downloads/supplementary_material-cvpr11-index-html/ > .